Impact of hydrogen isotope species on microinstabilities in helical plasmas

Impacts of hydrogen isotope species on microinstabilities in helical plasmas

Motoki NAKATA[1,2], **Masanori NUNAMI**[1,2], **Hideo SUGAMA**[1,2], **and Tomo-Hiko WATANABE**[3]

[1] National Institute for Fusion Science, Toki 509-5292, Japan
[2] Graduate University for Advanced Studies, Toki 509-5292, Japan
[3] Department of Physics, Nagoya University, Nagoya 464-8602, Japan

E-mail: nakata.motoki@nifs.ac.jp

Abstract. Impacts of isotope ion mass on ion-scale and electron-scale microinstabilities such as ion temperature gradient(ITG), trapped electron(TEM), and electron temperature gradient(ETG) modes in helical plasmas are investigated by using gyrokinetic Vlasov simulations with hydrogen isotope and real-mass kinetic electrons. Comprehensive scans for the equilibrium parameters and magnetic configurations clarify transition from ITG to TEM instability, where a significant TEM enhancement is revealed in the inward-shifted plasma case than that in the standard configuration. It is elucidated that the ion-mass dependence in the ratio of the electron-ion collision frequency to the ion transit one, i.e., $\nu_{ei}/\omega_{ti} \propto (m_i/m_e)^{1/2}$, leads to a stabilization of the TEM for heavier isotope ions. The ITG growth rate indicates a gyro-Bohm like ion-mass dependence, where the mixing-length estimate of diffusivity yields $\gamma/k_\perp^2 \propto m_i^{1/2}$. On the other hand, a weak isotope dependence of the ETG growth rate is identified. The collisionality scan also reveals that the TEM stabilization by the isotope ions becomes more significant for relatively higher collisionality in a banana regime.

1. Introduction

Understanding of microinstabilities and the resultant turbulent transport of energy and particle is one of the most important issues for the quantitative evaluation and prediction of confinement performance in magnetically confined fusion plasmas. In particular, since the burning plasmas in ITER and DEMO reactors are composed of mixture of hydrogen isotopes such as the deuterium and tritium, its impacts on the microinstabilities, turbulent transport, and zonal flows should be clarified for achieving better energy and particle confinements.

Experimental studies in tokamak devices such as ASDEX Upgrade[1] and JT-60U[2] have shown some clear evidences of the isotope effects on the confinement performance and the threshold power in L-H transition. Actually, in comparison with the hydrogen case, the energy confinement time in the deuterium plasma is much improved beyond the estimation of the gyro-Bohm scaling with the ion-mass dependence of $m_i^{1/2}$ for the confinement degradation, and the H-mode state is sustained with relatively lower threshold power[3]. In stellarator devices, a strong dependence of the statistical characteristics of turbulence on the isotope ion

mass has been recently observed in TJ-II experiments[4], where a relatively longer toroidal correlation length of electrostatic potential fluctuations is identified in a deuterium plasma with electron-root electric fields. The ion mass impact on the particle transport has also been investigated by density modulation experiments in Compact Helical System(CHS)[5]. However, the experimental identification of the improved energy confinement is still limited, e.g., W7-AS stellarator[6], and the forthcoming deuterium plasma experiments in Large Helical Device(LHD)[7] are expected to resolve the long-standing open issue in helical plasma researches.

In addition to the experimental studies, one should be also establish theoretical understanding for the detail physical mechanisms of the isotope effects on the ion-temperature-gradient(ITG), trapped-electron-mode(TEM), and the electron-temperature-gradient(ETG) instabilities, which are the fundamental causes of the electrostatic turbulence. Based on a gyrofluid model, Tokar *et al*. has shown that finite gyroradius effects enhanced by the isotope ion mass diminish the collisional TEM instability in tokamak geometry[8], and the associated transport model for the ITG and TEM has also been applied to 1D transport simulations of D-T mixture plasmas[9]. In this study, characteristics of the ion-scale and electron-scale micro instabilities in helical plasmas with model LHD configurations are clarified by the gyrokinetic simulation[10] which is the first-principle-based approach to examine the turbulent transport and zonal flows. We use the gyrokinetic Vlasov simulation GKV[11] with the hydrogen isotope species and real-mass kinetic electrons, where the roles of finite collisions are also examined beyond the conventional analyses in the collisionless limit[12, 13].

The rest of the paper is organized as follows. The gyrokinetic simulation model is presented in Sec. 2. Then, the parameter dependence of microinstabilities is shown in Sec. 3. In Sec. 4, the effects of the hydrogen isotope on the ITG, TEM, and ETG modes with finite collisions are discussed. Finally, the concluding remarks are given in Sec. 5.

2. Gyrokinetic Vlasov simulation model for helical plasmas

The simulation model in GKV are briefly presented in this section [see also Refs. [14, 15] for the details]. One of the governing equations is the electromagnetic gyrokinetic equation describing the time evolution of the perturbed gyrocenter distribution function $\delta f_{\rm s}^{\rm (g)}$ on the five-dimensional phase-space $(\boldsymbol{x}_{\rm g}, v_\parallel, \mu)$, where "s" is the particle species index. The Fourier form with the perpendicular wavenumber $\boldsymbol{k}_\perp$ is given by

$$\left(\frac{\partial}{\partial t} + v_\parallel \boldsymbol{b}\cdot\nabla + i\omega_{\rm Ds} - \frac{\mu \boldsymbol{b}\cdot\nabla B}{m_{\rm s}}\frac{\partial}{\partial v_\parallel}\right)\delta g_{{\rm s}\boldsymbol{k}_\perp} - \frac{c}{B}\sum_{\Delta} \boldsymbol{b}\cdot(\boldsymbol{k}'_\perp \times \boldsymbol{k}''_\perp)\,\delta\psi_{{\rm s}\boldsymbol{k}'_\perp}\delta g_{{\rm s}\boldsymbol{k}''_\perp}$$
$$= \frac{e_{\rm s}F_{\rm Ms}}{T_{\rm s}}\left(\frac{\partial \delta\psi_{\boldsymbol{k}_\perp}}{\partial t} + i\omega_{*T{\rm s}}\delta\psi_{\boldsymbol{k}_\perp}\right) + C_{\rm s}(\delta g_{{\rm s}\boldsymbol{k}_\perp}) \ , \qquad (1)$$

where $\delta g_{{\rm s}\boldsymbol{k}_\perp}$ stands for the non-adiabatic part, i.e., $\delta g_{{\rm s}\boldsymbol{k}_\perp} = \delta f^{\rm (g)}_{{\rm s}\boldsymbol{k}_\perp} + e_{\rm s}J_{0{\rm s}}\delta\phi_{\boldsymbol{k}_\perp}F_{\rm Ms}/T_{\rm s}$ with the local Maxwellian $F_{\rm Ms}$. The particle mass, the electric charge, the equilibrium temperature, and the gyrofrequency are denoted by $m_{\rm s}$, $e_{\rm s}$, $T_{\rm s}$, and $\Omega_{\rm s} = e_{\rm s}B/m_{\rm s}c$, respectively. The parallel

velocity $v_\parallel$ and the magnetic moment μ are used as the velocity-space coordinates, where μ is defined by $\mu = m_s v_\perp^2/2B$ with the perpendicular velocity $v_\perp$. The gyro-averaged potential fluctuation is denoted by $\delta\psi_{\boldsymbol{k}_\perp} = J_{0s}[\delta\phi_{\boldsymbol{k}_\perp} - (v_\parallel/c)\delta A_{\parallel\boldsymbol{k}_\perp}]$ with the zeroth-order Bessel function $J_{0s} = J_0(k_\perp v_\perp/\Omega_s)$, and the former and latter ones mean the electrostatic and electromagnetic parts, respectively. Here, we focus on electrostatic modes, but one finds a review of the electromagnetic analyses in Ref.[16].

Collisional effects are introduced in terms of a linearized model collision operator C_s, where a simplified Lenard-Bernstein model is applied here in order to perform the numerical scans for wide parameter regimes. The normalized collision frequency is defined as $\nu^*_{ss'} = qR_{ax}\tau_{ss'}^{-1}/(\sqrt{2}\epsilon^{3/2}v_{ts})$ with the characteristic collision time $\tau_{ss'}$, where q, R_{ax}, ϵ, and $v_{ts} = (T_s/m_s)^{1/2}$ represent the safety factor, the inverse aspect ratio, and the thermal speed, respectively. Recently, more accurate gyrokinetic multi-species collision operator, in which both the conservation properties and the Boltzmann's H-theorem are satisfied[17], has been implemented in GKV[18, 19].

The gyrokinetic equation shown in Eq. (1) is solved in the local flux-tube coordinates (x, y, z) defined as $x = a(\rho - \rho_0)$, $y = a\rho_0 q(\rho_0)^{-1}\left[q(\rho)\theta - \zeta\right]$, $z = \theta$ with the straight field line coordinates (ρ, θ, ζ), where a and $q(\rho_0)$ denote the plasma minor radius and the safety factor on the flux surface label of interest ρ_0, respectively. In these coordinates, the magnetic and diamagnetic drift frequencies are given by

$$\omega_{Ds} = \frac{c}{e_s B}\boldsymbol{k}_\perp\cdot\boldsymbol{b}\times\left(\mu\nabla B + m_s v_\parallel^2\boldsymbol{b}\cdot\nabla\boldsymbol{b}\right) = \frac{c(m_s v_\parallel^2+\mu B)}{e_s B_{ax}}\left(\mathcal{K}_x k_x + \mathcal{K}_y k_y\right), \tag{2}$$

$$\omega_{*Ts} = \frac{cT_s}{e_s B}\left[1 + \eta_s\left(\frac{m_s v_\parallel^2+2\mu B}{2T_s} - \frac{3}{2}\right)\right]\boldsymbol{k}_\perp\cdot\boldsymbol{b}\times\nabla\ln n_s, \tag{3}$$

where $\eta_s = L_{n_s}/L_{T_s}$ with $L_{n_s} = -(d\ln n_s/dx)^{-1}$ and $L_{T_s} = -(d\ln T_s/dx)^{-1}$ represents the ratio of density- to temperature-gradient scale length. The pressure gradient effect in the curvature drift is ignored by the low-β approximation.

In the present study, the geometric coefficients $\mathcal{K}_x$ and $\mathcal{K}_y$ defined with metric tensor components g^{ij} for $(i, j) = (x, y, z)$ are reduced to the so-called $s-\alpha$ limit [cf. Ref. [20]], and a model helical magnetic field[13, 14, 15] on Large Helical Device(LHD) with $L = 2$, $M = 10$ is considered, where the analytic form is given by

$$B = B_{ax}\left[1 - \epsilon_{00}(\rho) - \epsilon_t(\rho)\cos\theta - \sum_{l=L-1}^{l=L+1}\epsilon_l(\rho)\cos(l\theta - M\zeta)\right]. \tag{4}$$

The field intensity on the magnetic axis is denoted by B_{ax}, and the toroidal and helical ripple components are given by ϵ_{00}, ϵ_t, and ϵ_l, where their specific values are given in Ref. [14]. As shown in Fig. 1, two magnetic field configurations are considered, i.e., the standard configuration with $R_{ax} = 3.75$m (Std.) and an inward-shifted plasma case with $R_{ax} = 3.60$m (Iwd.) in which the neoclassical transport is reduced by decreasing the radial drift velocities of trapped particles[21].

The potential fluctuations are determined by the Poisson and Ampère equations:

$$\left(k_\perp^2 + \lambda_D^{-2}\right)\delta\phi_{\boldsymbol{k}_\perp} = 4\pi\sum_s e_s\int d\boldsymbol{v} J_{0s}\delta g_{s\boldsymbol{k}_\perp}, \tag{5}$$

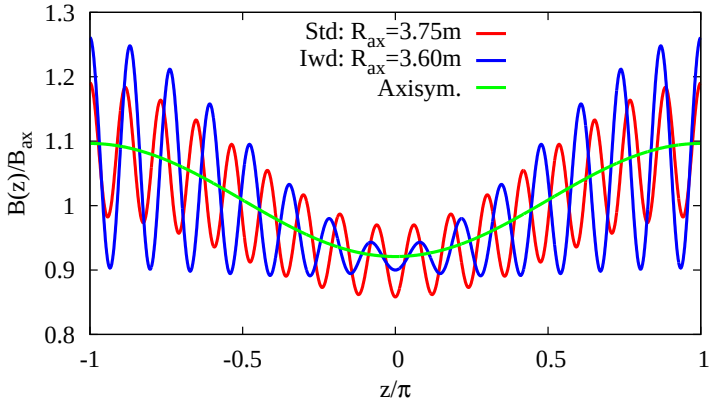

Figure 1. Magnetic field intensity along the field line for the standard (Std: $R_{\rm ax} = 3.75$m) and the inward-shifted (Iwd: $R_{\rm ax} = 3.60$m) plasma configurations, where the axisymmetric case is also plotted for comparison.

$$k_\perp^2 \delta A_{\parallel \boldsymbol{k}_\perp} = \frac{4\pi}{c} \sum_{\rm s} e_{\rm s} \int d\boldsymbol{v}\, v_\parallel J_{0{\rm s}} \delta g_{{\rm s}\boldsymbol{k}_\perp} \,, \tag{6}$$

where $\lambda_{\rm D} = (\sum_{\rm s} 4\pi n_{\rm s} e_{\rm s}^2/T_{\rm s})^{-1/2}$ is the Debye length. It is noted that, in the adiabatic electron limit with $k_\perp \rho_{\rm te} \ll 1$, the gyrocenter density fluctuation for electrons is approximated by $\int d\boldsymbol{v}\, J_{0{\rm e}} \delta f^{\rm (g)}_{{\rm e}\boldsymbol{k}_\perp} \simeq -e n_{\rm e} (\delta\phi_{\boldsymbol{k}_\perp} - \langle \delta\phi_{\boldsymbol{k}_\perp} \rangle_z \delta_{k_y,0})/T_{\rm e}$, where $\rho_{\rm ts} = m_{\rm s} c v_{\rm ts}/|e_{\rm s}| B_{\rm ax}$ means the gyroradius evaluated with the thermal speed $v_{\rm ts}$, and the field-line average is defined by $\langle X_{\boldsymbol{k}_\perp} \rangle_z = \int dz \sqrt{g}_{xyz} X_{\boldsymbol{k}_\perp} / \int dz \sqrt{g}_{xyz} \simeq \int dz\, B^{-1} X_{\boldsymbol{k}_\perp} / \int dz\, B^{-1}$. On the other hand, the ion density fluctuation is ignored in the adiabatic ion limit with $k_\perp \rho_{\rm ti} \gg 1$, i.e., $\int d\boldsymbol{v}\, J_{0{\rm i}} \delta f^{\rm (g)}_{{\rm i}\boldsymbol{k}_\perp} \simeq 0$.

3. Identification of ITG- and TEM-unstable parameter regime

The linear GKV simulation results on the electrostatic microinstabilities are presented in this section, where the hydrogen ions(s=H) and real-mass kinetic electrons(s=e) are solved in the simulation. Then, we identify the ITG- and TEM-unstable regimes depending on the magnetic configurations and equilibrium parameters, which cover a wide variety of the high-temperature discharges in the actual LHD experiments[7, 22]. Figures 2(a) and 2(b) show comparisons of the ITG and TEM growth rates in the standard magnetic configuration and the inward-shifted plasma cases, respectively, where the ion-temperature-gradient ($R_{\rm ax}/L_{T_{\rm i}}$) dependence of the linear growth rate γ for $k_x \rho_{\rm tH} = 0$ and $k_y \rho_{\rm tH} = 0.5$ is plotted. In analogy with tokamak cases, one can see transition of the dominant linear instability from ITG to TEM, depending on the ion-temperature gradient. The TEM growth rate strongly depends on the electron-temperature gradient while the ITG growth rate does not. The ITG growth rate in the inward-shifted plasma case is slightly enhanced in comparison with that in the standard configuration, but the reduction of the ITG-driven turbulent transport by enhanced zonal flows in the inward-shifted case has been pointed out[13, 23]. It is also stressed that the TEM instability is much enhanced in the inward-shifted case, where the helically trapped particle fraction in the electron distribution function increases.

The dependencies of the density gradient $R_{\rm ax}/L_n$ and the temperature ratio $T_{\rm e}/T_{\rm i}$ on the ITG and TEM instabilities are shown in Figs. 3(a) and 3(b), respectively, where $T_{\rm e}$ is changed under the fixed $T_{\rm i}$ here. One can see that both the ITG and TEM growth rates are proportional to $T_{\rm e}/T_{\rm i}$ and the magnitude of the positive $R_{\rm ax}/L_n$ corresponding to the peaked density profile. For the hollow density profile with $R_{\rm ax}/L_n < 0$, the TEM instability is completely stabilized, while the ITG case shows only slight decrease of the growth rate. It should be noted that such tendency of the TEM is qualitatively consistent with a theoretical evaluation for the unstable resonance between the drift waves and trapped-electron precessions, where the so-called maximum-J property with $\partial J/\partial\rho < 0$ (J: longitudinal adiabatic invariant) provides the stabilization of collisionless TEM for the peaked density profile with $dn_{\rm e}/d\rho < 0$, i.e., $\omega_{*T_{\rm e}}\langle\omega_{\rm De}\rangle_{\rm bounce} \propto -(\partial J/\partial\rho)(dn_{\rm e}/d\rho) < 0 \Longrightarrow \gamma_{\rm TEM} < 0$[24, 25]. Since the LHD-like helical magnetic configuration does not posses the maximum-J property, e.g., $\partial J/\partial\rho > 0$, the nearly flat or hollow density profile is favorable to stabilize the TEM instability.

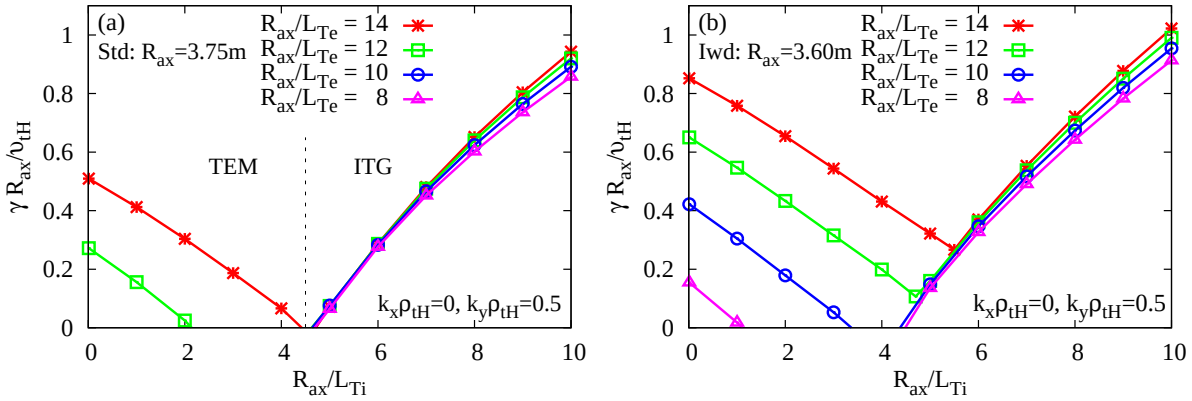

Figure 2. ITG and TEM growth rates in the hydrogen(s=H) helical plasma with (a)the standard and (b)inward-shifted configurations, where $R_{\rm ax}/L_n = 2$, $T_{\rm e}/T_{\rm i} = 2$, and $\nu^*_{\rm ei} \simeq 0.04$ are fixed.

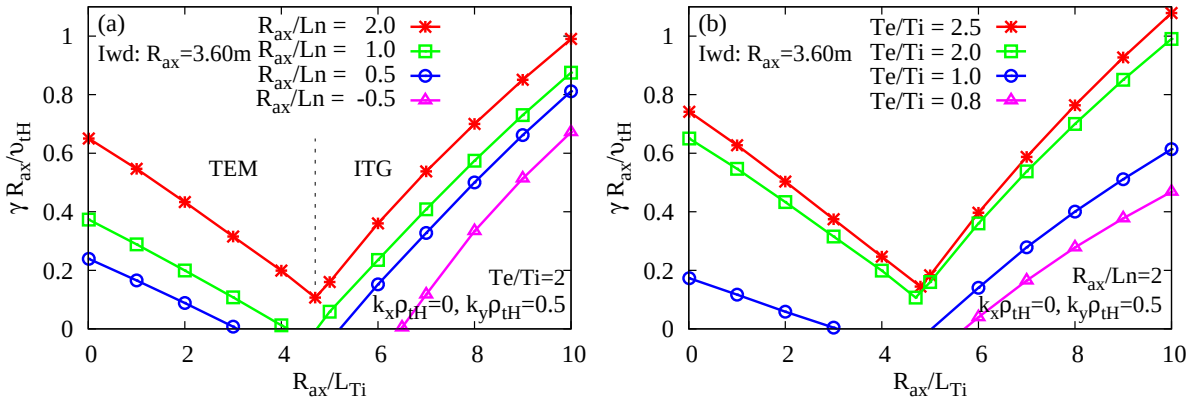

Figure 3. Parameter dependence of (a)the density gradient $R_{\rm ax}/L_n$ and (b)the temperature ratio $T_{\rm e}/T_{\rm i}$ on the ITG and TEM growth rates, where $R_{\rm ax}/L_{T_{\rm e}} = 12$ and $\nu^*_{\rm ei} \simeq 0.04$ are fixed.

4. Isotope ion mass impact on ion-scale and electron-scale modes with finite collisions

In this section, we discuss the impact of hydrogen isotope mass on the ion-scale (ITG and TEM) and electron-scale (ETG) instabilities with the finite collisions in helical plasmas, where the hydrogen(s=H), deuterium(s=D), and the tritium(s=T) species are considered. Here, ITG- and TEM-dominated parameter regimes shown in Fig. 3(b) are examined as the representative cases, where the equilibrium parameters used in the gyrokinetic simulation are $\{R_{\rm ax}/L_{T_{\rm i}} = 10,\ R_{\rm ax}/L_{T_{\rm e}} = 12,\ R_{\rm ax}/L_n = 2,\ T_{\rm e}/T_{\rm i} = 1\}$ for the ITG, and $\{R_{\rm ax}/L_{T_{\rm i}} = 1,\ R_{\rm ax}/L_{T_{\rm e}} = 12,\ R_{\rm ax}/L_n = 2,\ T_{\rm e}/T_{\rm i} = 2.5\}$ for the TEM. They correspond to profile conditions in the high-Ti[7] and high-Te[22] plasmas in LHD experiments, respectively. Note that the parameters used in the ETG case, which will be shown later, are the same as those in the TEM case.

Figures 4(a) and 4(b) show the normalized growth rate $\gamma R_{\rm ax}/v_{\rm ts}$ and the mode frequency $\omega_{\rm r} R_{\rm ax}/v_{\rm ts}$ as a function of the normalized wavenumber $k_y\rho_{\rm ts}$ for the ITG and TEM cases, respectively, where the thermal speed $v_{\rm ts}$ and gyroradius $\rho_{\rm ts}$ of each isotope ion with s={H, D, T} are used in the normalization. It is clarified that the TEM case shows a significant reduction of the normalized growth rate for the heavier isotope ions [Fig. 4(b)]. On the other hand, the ITG cases show almost the same profiles on $\gamma R_{\rm ax}/v_{\rm ts}$ [Fig. 4(a)], indicating a gyro-Bohm like ion-mass dependence, i.e., $\gamma/k_\perp^2 \propto m_{\rm s}^{1/2}$. Note that the normalized mode frequency is almost independent of the isotope species for both the ITG and TEM cases. The strong isotope dependence found in the TEM is attributed to the finite electron-ion collisions. Actually, even though the electron-ion collision frequency $\nu_{\rm ei} = \tau_{\rm ei}^{-1}$ does not depend on the ion mass, the collisional effect is effectively enhanced through the ion-mass dependence in the ratio of $\nu_{\rm ei}$ to the ion transit frequency $\omega_{\rm ti} = qR_{\rm ax}/v_{\rm ti}$, i.e., $\nu_{\rm ei}/\omega_{\rm ti} \propto (m_{\rm i}/m_{\rm e})^{1/2}$, which is an essential factor for the stabilization of the collisionless TEM. Note that the stabilization effect on the ITG by the ion-ion collisions is almost independent of the ion mass, i.e., $\nu_{\rm ii}/\omega_{\rm ti} \propto m_{\rm i}^0$.

The isotope effects on the electron-scale instability are also investigated, where the wavenumber spectra of γ and $\omega_{\rm r}$ normalized by the electron thermal speed $v_{\rm te}$ and the

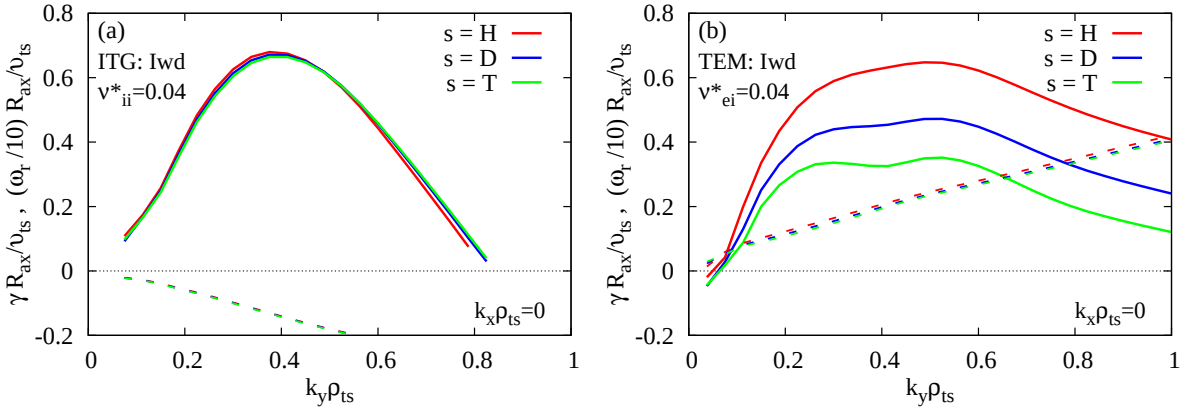

Figure 4. Comparison of the normalized linear growth rate $\gamma R_{\rm ax}/v_{\rm ts}$(solid) and mode frequency $\omega_{\rm r} R_{\rm ax}/v_{\rm ts}$(dashed) in (a)ITG and (b)TEM instabilities with the hydrogen isotope species.

gyroradius ρ_{te} in the TEM-ETG modes are shown in Fig. 5(a). In the present analyses, the stabilization effects due to $T_e/T_i > 1$ and the finite Debye length lead to a near-marginal ETG instability with the moderate growth rate. Unlike in the ITG cases showing a gyro-Bohm like dependence, a weak isotope dependence appears in the ETG growth rate with two peaks at $k_y\rho_{te} = 0.1$ and $k_y\rho_{te} = 0.175$, where the result with the adiabatic ion approximation in $m_i/m_e \to \infty$ is also plotted for comparisons. From comparisons with adiabatic-ion cases, one finds that the kinetic ion responses destabilize the TEM and/or ETG for $k_y\rho_{te} \simeq 0.057$ [dashed lines in Figs. 5(c) and 5(d)], and make the ETG growth rate larger in the higher wavenumber region, where their eigen-mode structures expanded in the z-direction are shown in Fig. 5(b).

Figures 6 show the collisionality dependence of the normalized growth rate of the ITG, TEM and ETG modes, where the equilibrium density is changed in the collision frequency. The normalized growth rate $\gamma R_{ax}/v_{ts}$(s = H, D, T) or $\gamma R_{ax}/v_{te}$ in the ITG and ETG modes indicates only weak ion-mass dependence[cf. Figs. 4(a) and 5(a)] through ν^*_{ii} or ν^*_{ee}. On the other hand, it is revealed that the normalized TEM growth rate strongly depends on ν^*_{ei}, and then the stabilization by the isotope ion mass is significant in relatively higher collisionality regimes, but still within a banana regime. Indeed, as stated above, the finite collision effect leads to the isotope dependence of the TEM growth rate, while one finds almost no isotope dependence on the normalized growth rates for all the instabilities in the collisionless limit.

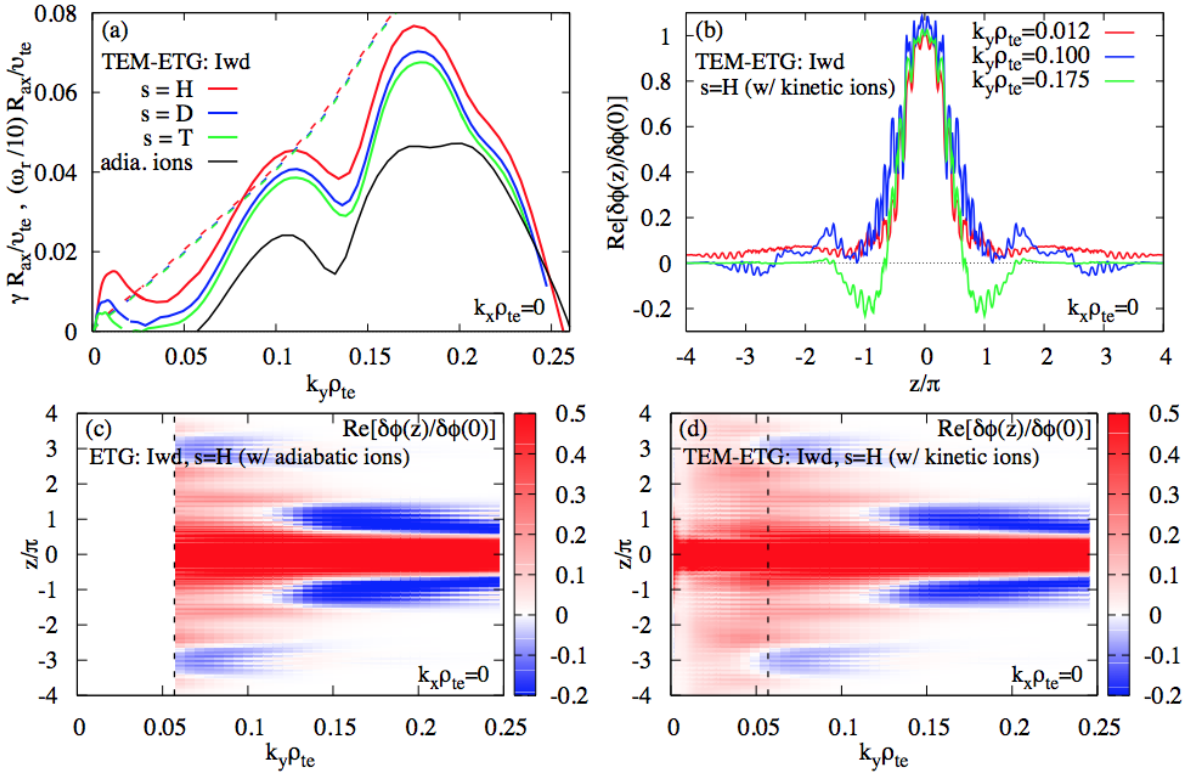

Figure 5. (a)The growth rate(solid) and the mode frequency(dashed) in ETG modes, (b)the real part of eigen-mode structures in the field-line direction z, and the (k_y, z)-contour map of the real part of eigen-modes for (c)adiabatic-ion and (d)kinetic-ion cases.

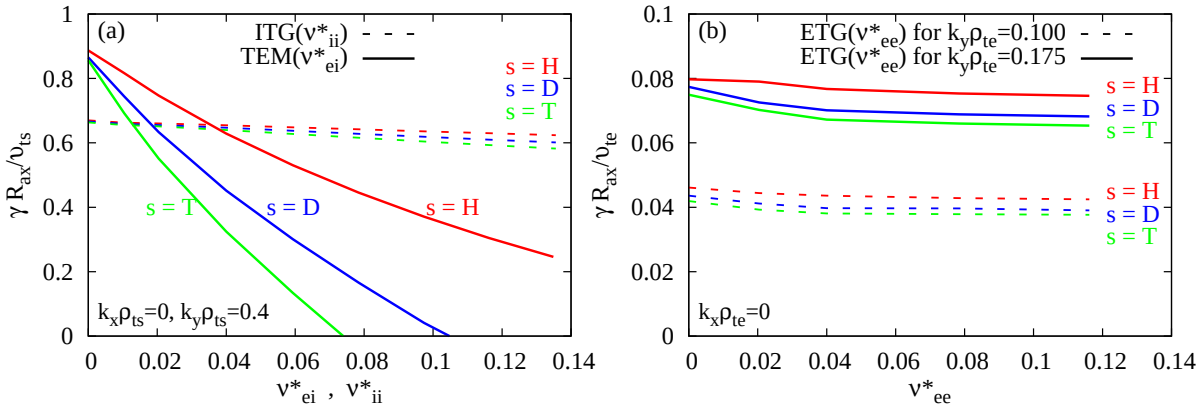

Figure 6. Collisionality dependence of the normalized (a)ITG(dashed) and TEM(solid) growth rates, and (b)ETG-growth rate at $k_y\rho_{te} = 0.1$(dashed) and $k_y\rho_{te} = 0.175$(solid).

5. Concluding remarks

Electrostatic microinstabilities in helical plasmas with LHD configurations are investigated by using the gyrokinetic Vlasov simulation GKV with hydrogen isotope species and real-mass kinetic electrons. Comprehensive scans for the equilibrium parameters provide one with the ITG- and TEM-stability properties, including the magnetic-configuration dependence such as the standard and inward-shifted plasma configurations. Then, distinct differences in the density gradient dependence are revealed in the ITG and TEM cases, i.e., the TEM can be stabilized in the hollow density profile whereas the ITG modes remain unstable.

The impacts of hydrogen isotope species on the ITG, TEM, and ETG modes are examined. It is found that the significant isotope dependence appears as reduction of the TEM growth rate, while the ITG case indicates a gyro-Bohm like ion-mass dependence, where the mixing-length diffusivity yields $\gamma/k_\perp^2 \propto m_i^{1/2}$. On the other hand, a weak dependence of the ETG growth rate on the isotope ion-mass is identified. The strong isotope effect in the TEM stems from the ion-mass dependence of the ratio of the electron-ion collision frequency to the ion transit frequency $\nu_{ei}/\omega_{ti} \propto (m_i/m_e)^{1/2}$, which is essential for the stabilization of the collisionless TEM. Also, the collisionality scan reveals that the TEM stabilization by the isotope ion mass becomes more significant in relatively higher collisionality regimes.

Since the similar mechanism exists in tokamaks[8, 26] and the other stellarators, the TEM stabilization by hydrogen isotope provides us with fruitful insights into high-T_e operations in the experiments and future reactors. The present analysis based on the gyrokinetic model without mean poloidal and toroidal rotations show the weak isotope impact on the ITG modes. However, one should note that the reduction of the ITG-driven turbulent transport can be expected through the zonal-flow enhancement by the mean poloidal rotation depending on the ion mass in a helical system[27, 28]. The TEM- and ITG-driven turbulence and zonal flows in helical plasmas with isotope species should be investigated by means of nonlinear gyrokinetic simulations, and the results will be reported elsewhere.

Acknowledgments

The authors would like to thank Drs. J. H. E. Proll (IPP-Greifswald) and K. Tanaka (NIFS) for fruitful discussions on this study. Numerical simulations were performed by Plasma Simulator at NIFS, and HELIOS at IFERC-CSC. This work is supported by the MEXT Japan, Grant Nos. 26820401, in part by the NIFS collaborative Research Programs (NIFS14KNTT026, NIFS14KNST065, NIFS15KNST085, NIFS15KNTT031, NIFS16KNST096), and in part by the MEXT grant for Post-K project: Development of innovative clean energy, Core design of fusion reactor.

References

[1] M. Bessenrodt-Weberparl *et al*., Nucl. Fusion 33, 1205 (1993)
[2] H. Urano *et al*., Phys. Rev. Lett. 109 125001 (2012)
[3] H. Urano *et al*., Nucl. Fusion 53 083003 (2013)
[4] B. Liu *et al*., Nucl. Fusion 55 112002 (2015)
[5] K. Tanaka *et al*., Plasma Phys. Control. Fusion 58 055011 (2016)
[6] U. Stroth *et al*., Physica Scripta 51 655 (1995)
[7] K. Nagaoka *et al*., Nucl. Fusion 55 113020 (2015)
[8] M. Z. Tokar *et al*., Phys. Rev. Lett. 92 215001 (2004)
[9] M. Z. Tokar *et al*., Nucl. Fusion 51 063013 (2011)
[10] X. Garbet *et al*., Nucl. Fusion 50, 043002 (2010)
[11] T. -H. Watanabe *et al*., Nucl. Fusion 46, 24 (2006)
[12] O. Yamagishi *et al*., Phys. Plasmas 14, 012505 (2007)
[13] S. Ferrando *et al*., Phys. Plasmas 14, 122505 (2007)
[14] T. -H. Watanabe *et al*., Nucl. Fusion 47, 1383 (2007)
[15] M. Nunami *et al*., Plasma Fusion Res. 5, 016 (2010)
[16] A. Ishizawa *et al*., J. Plasma Physics 81, 435810203 (2015)
[17] H. Sugama *et al*., Phys. Plasmas 16, 112502 (2009)
[18] M. Nakata *et al*., Comput. Phys. Commun. 197, 61 (2015)
[19] M. Nunami *et al*., Plasma Fusion. Res. 10, 1403058 (2015)
[20] M. Nakata *et al*., Plasma Fusion Res. 9, 1403029 (2014)
[21] S. Murakami *et al*., Nucl. Fusion 42 L19 (2002)
[22] H. Takahashi *et al*., Phys. Plasmas 21, 061506 (2014)
[23] T. -H. Watanabe *et al*., Phys. Rev. Lett. 100, 195002 (2008)
[24] P. Helander *et al*., Plasma Phys. Control. Fusion 54 124009 (2012)
[25] J. H. E. Proll *et al*., Phys. Rev. Lett. 108, 245002 (2012)
[26] I. Pusztai *et al*., Phys. Plasmas 18, 122501 (2011)
[27] H. Sugama *et al*., Phys. Plasmas 16, 056101 (2009)
[28] T. -H. Watanabe *et al*., Nucl. Fusion 51 123003 (2011)